Heliyon 10 (2024) e27714

Contents lists available at ScienceDirect

Heliyon

journal homepage: www.cell.com/heliyon

Research article

Microstructural characterization and corrosion-resistance behavior of friction stir-welded A390/10 wt% SiC composites-AA2024 Al alloy joints

Hamed Jamshidi Aval [a,*], Ivan Galvão [b]

[a] Department of Materials Engineering, Babol Noshirvani University of Technology, Shariati Avenue, Babol, 47148-71167, Iran
[b] Instituto Superior de Engenharia de Lisboa (ISEL), Departamento de Engenharia Mecânica, Instituto Politécnico de Lisboa, Rua Conselheiro Emídio Navarro 1, 1959-007 Lisboa, Portugal

ARTICLE INFO

Keywords:
Al-16Si–4Cu–10SiC composite
Al–4Cu–Mg alloy
Corrosion resistance
Dissimilar friction stir welding

ABSTRACT

This study examined the effect of traverse speed on the mechanical properties, corrosion-resistance behavior, and microstructure of friction stir-welded A390/10 wt% SiC composites-AA2024 Al alloy joints. The laminar flow of both materials was found to diminish in the stir zone (SZ) when the traverse speed of the tool increased from 40 to 80 mm/min, lowering their mixing rate. Large aspect ratio Si particles are broken by the tool pin-induced applied plastic strain, which turns them into refined equiaxed particles. Their aspect ratio remains unchanged in the SZ, despite their decreasing size. SiC and Si particles progressively come into view when moving from the AA2024 alloy's SZ to the composite workpieces. These changes happen abruptly as traverse speed increases due to the lack of an interfacial layer structure. The advancing side (AS)'s SZ grain size drops from 4.2 ± 0.3 μm to 1.2 ± 0.2 μm as the traverse speed drops from 80 to 40 mm/min. Increased traverse speed from 40 to 80 mm/min will result in a 5.8% decrease in elongation percentage (EP) and 8.4%, 36%, and 10.3% increases in the ultimate tensile strength (UTS), corrosion resistance, and yield strength, respectively.

1. Introduction

Aluminum matrix composites (AMCs) are a class of materials that have recently come into existence with certain properties, including low density and coefficient of thermal expansion (CTE) as well as high strength, specific modulus, and wear resistance. Composite material welding is not without its challenges. Reinforcement agglomeration and intermetallic phase formation potential should be considered while welding, which can degrade the quality of the resulting joint in certain situations. Certain researchers have reported on the fusion welding of particle-reinforced AMCs [1]. Even though these materials are destroyed by conventional fusion welding techniques, ceramic particles formed in the weld result in issues that can increase melt viscosity, create residual stresses because of various CTEs, and cause particle separation during cooling. Consequently, composites can be welded using solid-state welding techniques, which also helps tackle the aforementioned issues.

One solid-state welding technique used to join metal alloys—primarily Al—is FRICTION STIR WELDING (FSW). Joining of Al alloys is becoming increasingly important as Al consumption rises across many industries, aviation chief among them. Originally designed for

* Corresponding author.
E-mail addresses: h.jamshidi@nit.ac.ir (H. Jamshidi Aval), ivan.galvao@isel.pt (I. Galvão).

https://doi.org/10.1016/j.heliyon.2024.e27714
Received 13 October 2023; Received in revised form 5 March 2024; Accepted 5 March 2024
Available online 11 March 2024

Al alloys, this process is now applicable to polymers and steels as well. With the flexibility to come up with new designs, this welding technique has made it possible to produce joints that are both affordable and of excellent quality. Additionally, defects like porosity, slag inclusions, and solidification cracks reduce the joint's quality and characteristics when joining Al alloys by fusion welding. Notably, although solid-state welding techniques, e.g., FSW, deal with a number of issues with AMC fusion welding, such as porosity, distortion, cracking, and reinforcement particle dissolution, these materials have a narrower welding window than Al alloys when applying the FSW process due to particle reinforcement.

Few research studies have reported the FSW of AMCs [1–4]. The mechanical properties and microstructure of post-FSW AA6092 Al alloy matrix composite reinforced with SiC particles were examined by Salih et al. [5]. The findings demonstrated that the welded parts had developed relatively high ductility in addition to enhanced fatigue life due to forming refined equiaxed grains. The impact of the tool angle on the mechanical properties and microstructure of the AA6092 matrix composite reinforced with SiC particles was explored by Acharya et al. [1]. The findings demonstrated that, although a sound joint forms in the tool tilt angle range up to 2°, the joint strength increases from 1° to 2° and decreases thereafter. The impact of FSW on the mechanical properties and microstructure of the AA6063/SiC composite was also studied by Kaushik and Singhal [6]. According to the microstructural analysis, FSW significantly reduces the reinforcement size and ensures that it is distributed uniformly throughout the stir zone (SZ).

The mechanical properties and microstructural changes of the post-FSW AA6061/SiC composite were investigated by Kumar et al. [7]. The findings suggested that, besides traverse and tool rotational speed, the tool tilt angle is another critical factor in deciding the joint strength. The FSW of a B_4C-reinforced AMC was analyzed by Kalaiselvan et al. [8]. The findings demonstrated that, even under conditions of severe plastic deformation (SPD), refined equiaxed grains form when B_4C particles are uniformly distributed throughout the SZ, and the composite plasticity decreases upon welding. The FSW of a TiC-reinforced AMC was reviewed by Gopalakrishnan and Murugan [9]. According to the findings, the joint strength is 90–98% that of the base metal after it has been established. Additionally, the welding speed and tool pin profile were found to have a greater impact on the joint's tensile strength than other factors. The impact of the parameters of the FSW process on the wear behavior of an AMC reinforced with SiC particles was explored by Adel Mahmood et al. [10]. The findings demonstrated that the microstructural alterations brought about by the welding process factors enhance the welding zone (WZ) hardness and wear characteristics and have a major impact on the joints' wear resistance. The mechanical properties and microstructure of an FS-welded A356/SiC composite were inspected by Amirizad et al. [2]. The results demonstrated that, in comparison to the original composite, the microstructural alterations in the SZ enhance the mechanical properties, including elongation, hardness, yield strength, modulus of elasticity, and ultimate tensile strength (UTS). The impact of the FSW process on the AA2124/SiC composite's joint strength was explored by Bozkurt et al. [3]. The findings indicated that the joint strength decreases by enhancing the tool's traverse speed.

As previously mentioned, some researchers have looked into Al composite welding. The suitability for joining AMCs with other metals is a prerequisite for further applications. The current literature does not include any research on the dissimilar AMC-Al alloy joints. The aviation industry makes extensive use of AA2024 Al alloy owing to its high strength, which is achieved via a precipitation

Fig. 1. The dimensions of FSW tool used in this study.

hardening mechanism. AMCs can be fabricated in a variety of ways, including fusion welding. The transportation industry makes extensive use of Al-silicon (Si) hypereutectic alloys like A390 because of their excellent wear resistance and hardness, low CTE, good castability, and high temperature strength [11]. Utilizing Al–Si hypereutectic alloys to create AMC allows for the creation of a composite with exceptional strength-to-weight ratio, high modulus of elasticity, and excellent wear resistance. To capitalize on the AMC and Al alloy properties, these two materials were combined herein using FSW. This study examined the impact of traverse speed on the dissimilar FSW (DFSW) between the A390/10 wt% SiC composite and the AA2024 Al alloy.

2. Experimental procedures

According to earlier research, stir casting was used herein to prepare the A390/10 wt% SiC composite [12]. Sheets of the A390/10 wt% SiC composite were cast, each measuring 6 mm in thickness. The chemical composition of the A390 ingot was 4.1% Cu, 0.11% Fe, 16.18% Si, 0.09% Zn, 0.48% Mg, 0.08% Ti, 0.02% Mn, and Al balance (wt%). Additionally, a 6-mm AA2024-T4 Al alloy sheet with a chemical composition of 0.14% Si, 1.45% Mg, 4.14% Cu, 0.49% Mn, 0.26% Fe, and Al balance (wt%) was utilized herein to create a dissimilar joint. After machining the sheet edges, joining was completed by employing a welding machine operated under position control while the FSW procedure was followed. The composite and AA2024 Al alloy sheets were positioned on the AS and RS, respectively. As sown in Fig. 1, a WC tool with an 18 mm diameter and a screw cylindrical pin was used for welding. Four traverse speeds—40, 60, and 80 mm/min—and an 800-rpm rotational speed were used during the welding process. Based on initial testing, which involved a 400–1600 rpm rotational speed range and a 20–100 mm/min traverse speed range, the best results for a sound weld without a groove on the weld's crown side were obtained at 800 rpm rotational speed and 40, 60, and 80 mm/min traverse speed. Thus, samples coated with the aforementioned parameters were the subject of further investigations. A K-type thermocouple was inserted into the joint line to monitor the temperature during the welding process, and a thermocouple was utilized to calculate the SZ temperature. The welded samples were labeled as follows: V-40 for 40 mm/min, V-60 for 60 mm/min, and V-80 for 80 mm/min traverse speeds.

Fig. 2 illustrates that various samples were taken from the welded sample upon welding to determine the joint's mechanical properties and microstructure. As shown, the test samples for corrosion, mechanical properties, and microstructure were taken from the same location in various welded samples to maintain reproducibility. The welded samples' cross-section was polished with an alumina polishing suspension after being ground with SiC sandpaper to examine the microstructure. The microstructure was exposed through the use of the modified Keller's [reagent] etchant solution, which consisted of 150 ml H_2O, 6 ml HF, 6 ml HCl, and 3 ml HNO_3. A TESCAN MIRA3 field emission scanning electron microscope (FESEM) and an NGF-120A optical microscope were used to analyze the microstructure of various samples. As per ASTM E112-13, the linear intercept (LI) method was used to determine the grain sizes. Ten microstructural images and Clemex [automated] image analysis software were employed to calculate the precipitate and grain size. The samples' micro-Vickers hardness was calculated by utilizing a microhardness tester along the joint midsection perpendicular to the welding direction with a 10-s dwell time and a 100-g load. A universal testing machine (STM-250, SANTAM) was employed to assess the samples' tensile properties at a 1 mm/min cross-head speed as per ASTM E8 guidelines. Tensile test sample elongation was measured using an Instron extensometer. Both transverse and longitudinal tensile specimens were extracted from the welded samples with a 32 mm gauge length, of which 3 were prepared from each welded sample to ensure that the tensile test results were reproducible. A SEM was used to examine the fracture surface following the tensile test.

Polarization [index] (PI) testing was performed at 37 °C to examine the corrosion resistance of various samples in the NaCl solution. To prepare a NaCl solution (3.5 wt%), NaCl (35 g) was dissolved in double-distilled water (ddH_2O) to which NaOH (0.4 g) was added to keep the pH of the electrolyte at 10. The electrochemical tests, such as potentiodynamic polarization (PDP) and electrochemical

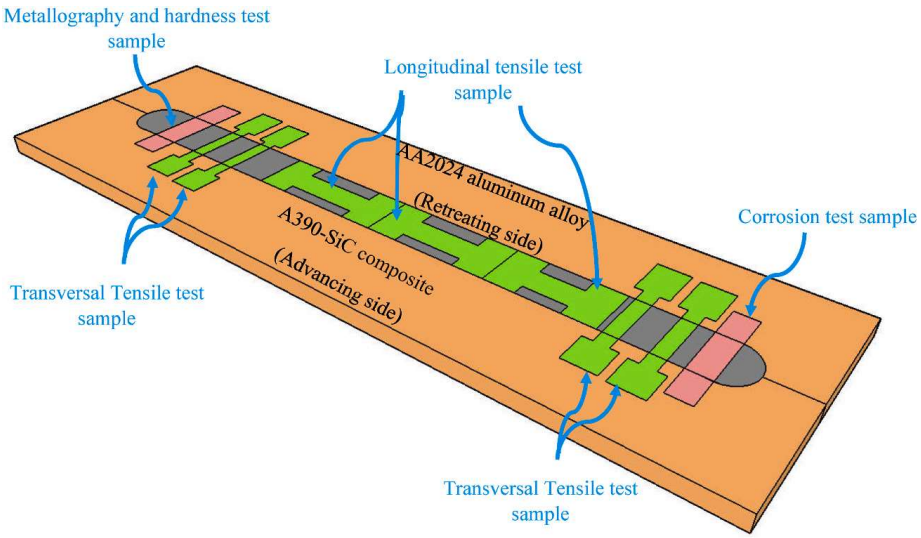

Fig. 2. The schematic view of the metallography, corrosion test, and tensile test sample extracting position.

impedance spectroscopy (EIS), were conducted using the Autolab electrochemical workstation model PGSTA 204. To achieve a steady state (with variations of lower than 5 mV every 5 min), samples were submerged in the NaCl solution for 1 h prior to each experiment. PDP was measured in the OCP potential range of 0.2V to −0.2V. To guarantee the reproducibility of the corrosion test results, 3 corrosion samples were made from each of the welded samples. After the corrosion test, a SEM was used to examine the corroded surface.

3. Results and discussion

The joint cross-section in all samples, each with a sound SZ, is displayed in Fig. 3(a–c). The amount of mixing between two base metals is reduced as the traverse speed of the tool increases. The sample welded with the lowest traverse speed clearly displays both materials' laminar flow in the SZ. Effective laminar flow formation can be achieved by mixing the two materials and allowing elements to diffuse at the layer interface. The difference between the velocity vectors on the retreating and ASs increases with an increase in the traverse speed. Non-uniform flow forms in the SZ under these conditions, while a layer interface does not form in the SZ due to a uniform flow. The thermo-mechanically affected zone (TMAZ), SZ, and base metals' microstructural images are displayed in Fig. 4 (a–e) to help with the analysis of the joint area's microstructural developments. All three welded samples have uniformly distributed SiC and Si particles in the SZ, which are smaller in size compared to the composite base metal. Large aspect ratio Si particles are indeed broken and transformed into refined equiaxed particles under tool-pin-induced applied plastic strain. The SiC particles' aspect ratio does not differ in the SZ despite their decreasing size. The composite base metal's SiC particles have an average size of 15.3 ± 2.1 μm, which are reduced to 6.5 ± 1.1, 5.4 ± 1.2, and 4.3 ± 0.9 μm, respectively, in the V-40, V-60, and V-80 samples. In the process, large aspect ratio eutectic Si is broken in Si particles, resulting in a reduction in its aspect ratio. Even though the primary Si particles have a polygonal morphology and a relatively constant aspect ratio, these particles only fracture and fragment into smaller particles.

Refined equiaxed grains formed in the AA2024 side's SZ. SiC and Si particles become gradually visible when the AA2024 alloy's SZ

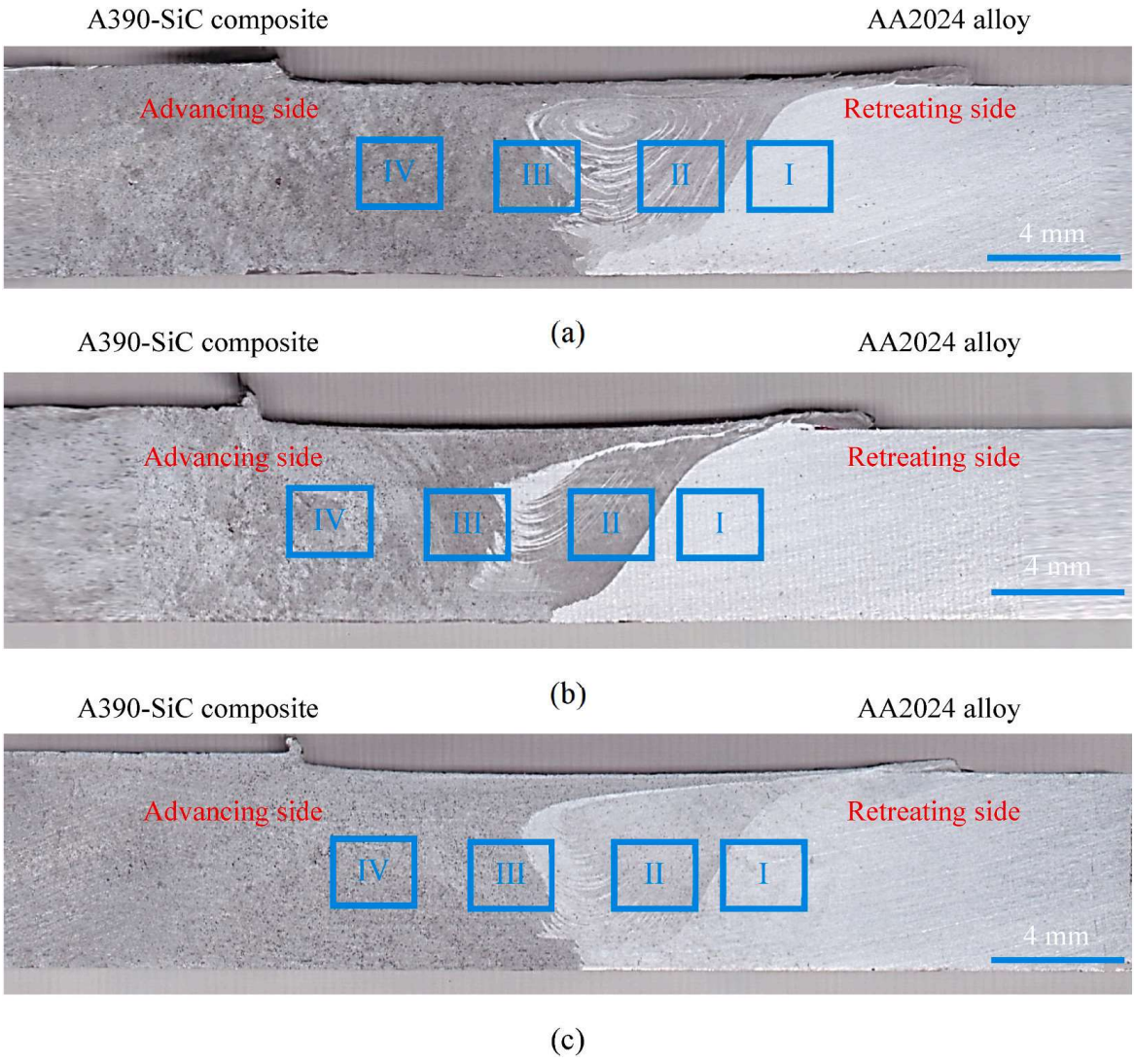

Fig. 3. Macrograph of cross section of different samples; a) V-40, b) V-60, c) V-80.

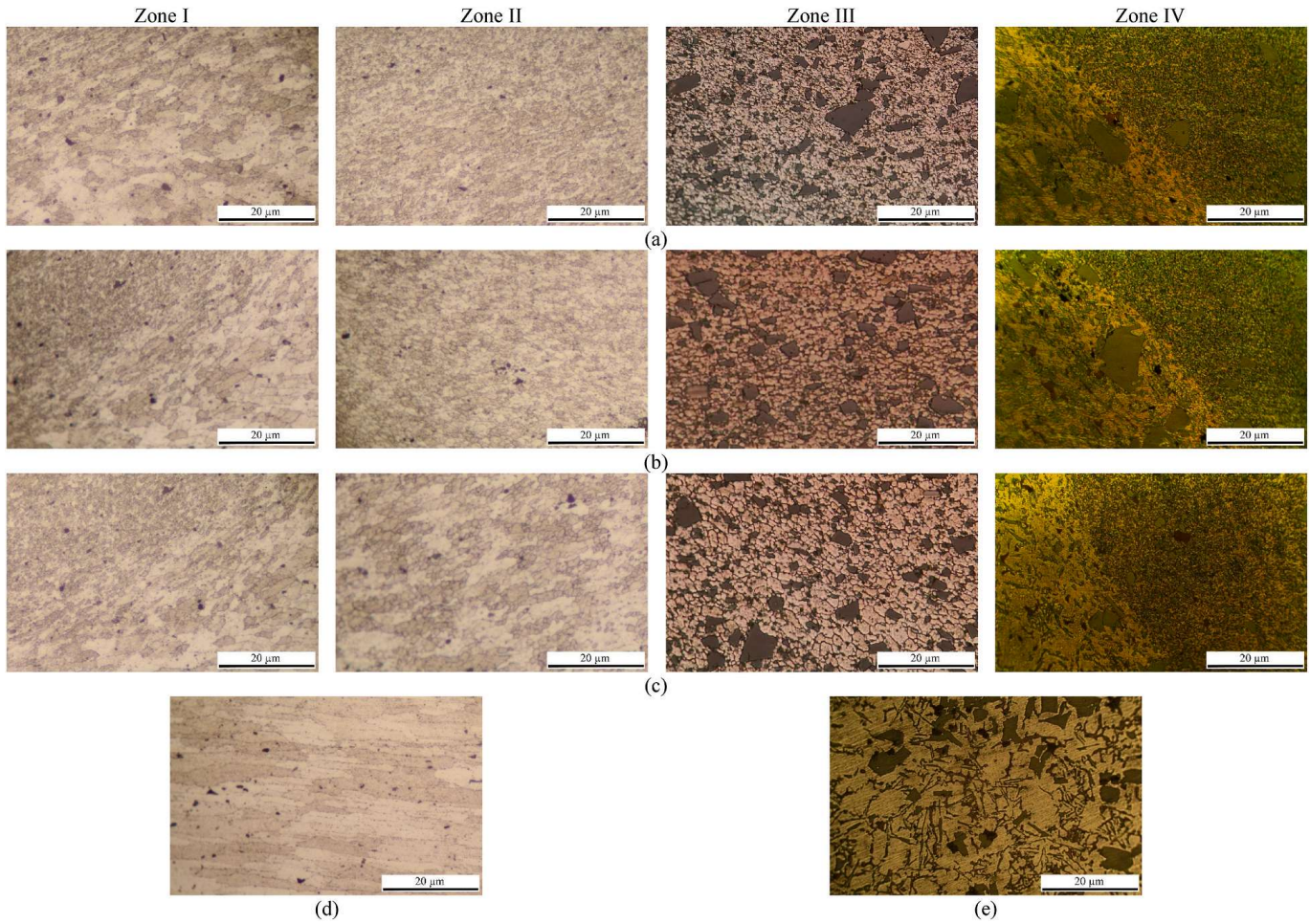

Fig. 4. Microstructure of different zones marked in Fig. 3; a) sample V-40, b) sample V-60, c) sample V-80, d) AA2024 base metal, e) A390-SiC composite base metal (Zone I = TMAZ of AA2024 side, Zone II = stir zone of AA2024 side, Zone III = stir zone of composite side, Zone IV = TMAZ of composite side).

transitions to the composite workpieces. The abruptness of these changes is ascribed to the absence of an interfacial layer structure, which causes increased traverse speed. Particles in the TMAZ are oriented and have elongated grains. Elongated grains are clearly visible on the AS, which agrees with findings obtained in other works [13,14].

Based on [15–17], the SZ experiences dynamic recrystallization during the process, which causes refined equiaxed grains to form there. The average grain size in AS (1.2 ± 0.2, 3.1 ± 0.1, and 4.2 ± 0.3 μm for V-40, V-60, and V-80 samples, respectively) is smaller than that in RS (1.5 ± 0.4, 3.4 ± 0.2, and 5.1 ± 0.2 μm for V-40, V-60, and V-80 samples, respectively). Also, based on [18–20], the AS experiences higher plastic strain and temperature than the RS during the welding process, which leads to the formation of recrystallized grains. The temperature drops and the plastic strain rises with decreasing recrystallized grain size. The effective formation of nucleation sites for recrystallized grains and inhibition of grain growth is facilitated by second-phase particles (SPPs), besides plastic strain and temperature. Finer grain formation may be mediated by high plastic strain and Si particles on the AS.

Conversely, when temperature rises but traverse speed falls, plastic strain increases and grain size diminishes because of the smaller particles in the SZ. Based on [21], the V-40, V-60, and V-80 sample SZ's plastic strain values are 25.6, 20.3, and 16.7 s^{-1}, respectively. Plastic strain and particle-stimulated nucleation help form refined grains in the SZ.

Precipitation-hardening alloys include two alloys, A390 and AA2024, whose respective strengths are effectively increased by S–Al_2CuMg and Θ-Al_2Cu precipitates. The evolution of aforementioned precipitates during welding can be studied based on the SZ's SEM images on both the AS and RS of various samples as well as those of the base metals, as depicted in Fig. 5(a–c) and 6 (a-c). The EDS analysis indicates that the composite base metal's microstructure constitutes SiC particles, Fe- and Cu-rich (Al_2Cu) precipitates and particles, and primary and eutectic Si particles. Besides, the AA2024 Al alloy's microstructure comprises Fe- and Cu-rich (Al_2CuMg) precipitates. The above images demonstrate that the types of precipitates and SPPs in the SZ remain unchanged from those of the base metals following welding. The SZ shows a substantial difference in S–Al_2CuMg and Θ-Al_2Cu precipitate formation, which are smaller in size than the base metal. S–Al_2CuMg and Θ-Al_2Cu precipitates dissolve at 350 and 300 °C, respectively [22,23]. Based on the SZ temperature of both samples, it can be inferred that S and Θ precipitates in the SZ dissolve under plastic strain and heat and then re-precipitate during cooling. Reduced traverse speed and joint cooling rate and elevated SZ temperature appear to cause the formed precipitates in the SZ to enlarge and grow more than those formed in the SZ of the welded sample at the highest traverse speed (i.e., 80

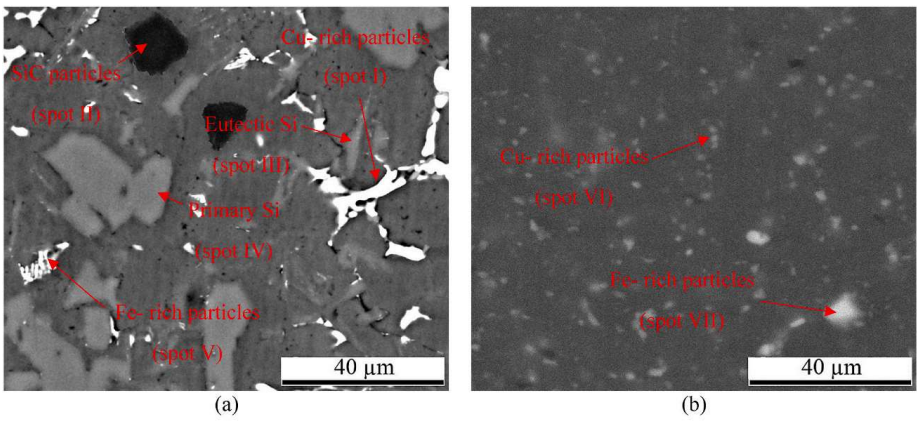

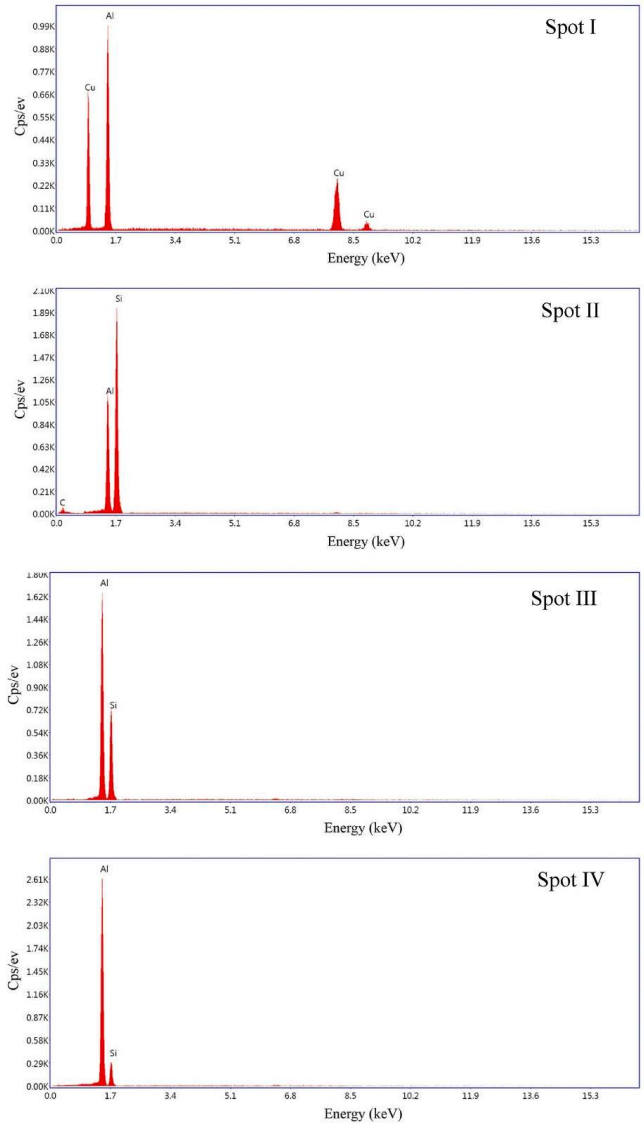

Fig. 5. Microstructure of; a) A390-10 wt%SiC composite base metal, b) AA2024 aluminum alloy base metal, c) EDS results of different points marked in Fig. 5 (a) and (b).

mm/min). Fig. 7 depicts the distribution coefficient graph along with the mean size of Si particles and S and Θ precipitates in the SZ of various samples. While S and Θ precipitates and Si particles are uniformly distributed in the SZ of all the samples, the mean size of Si particles is reduced (from 7.4 ± 0.9 to 5.9 ± 0.6 µm) with an increase in the shear stress and traverse speed (from 40 to 80 mm/min) in the SZ.

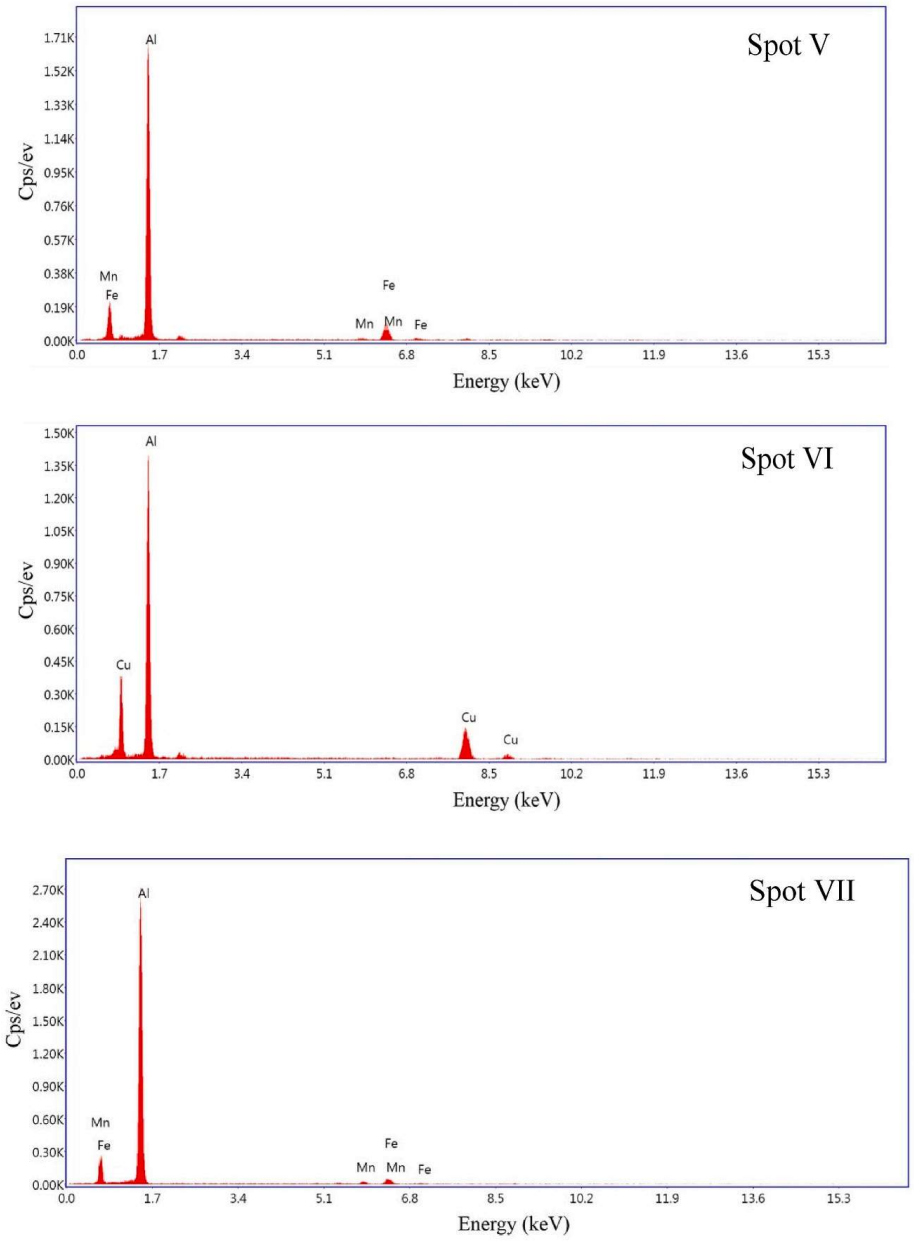

(c)

Fig. 5. (*continued*).

Fig. 8 displays the hardness profiles of various samples, where hardness changes take the shape of the letter M. Thus, the hardness of AA2024 decreases as it moves from the base metal side to the SZ and then increases in the SZ once more after passing through the TMAZ. Hardness declines once more when approaching the composite base metal's TMAZ, varying around the mean value 103 HV0.1. AA2024 is a precipitation-hardening alloy. Besides, applying heat may cause precipitate growth or dissolution, resulting in reduced hardness of this alloy's TMAZ. However, in contrast to what has been documented in earlier research, the presence of Si particles in the SZ on the AA2024 side can prevent its hardness from decreasing, leading to increased base metal hardness [24]. In comparison to the composite base metal, there is a notable increase in hardness in the composite side SZ because of the formation of smaller precipitates rich in copper and finer Si particles.

The results of the tensile test (Fig. 9(a–c)) indicate that while transverse tensile samples' elongation and strength values do not significantly differ, the transverse tensile test's strength values decrease as traverse speed decreases while elongation increases. The transverse tensile sample fracture happened in the TMAZ on the composite base metal side (Fig. 9 (c)). A considerable stress gradient occurs in the transition zone from the TMAZ because of the high hardness difference between the composite base metal and the SZ, along with other properties. This leads to fractures in the TMAZ. The longitudinal tensile test results show that the samples' tensile strength increases and their elongation percentage (EP) decreases when the traverse speed is increased from 40 to 80 mm/min. The likelihood of the formation of finer precipitates increases with increased traverse speed and decreased heat application to the welding

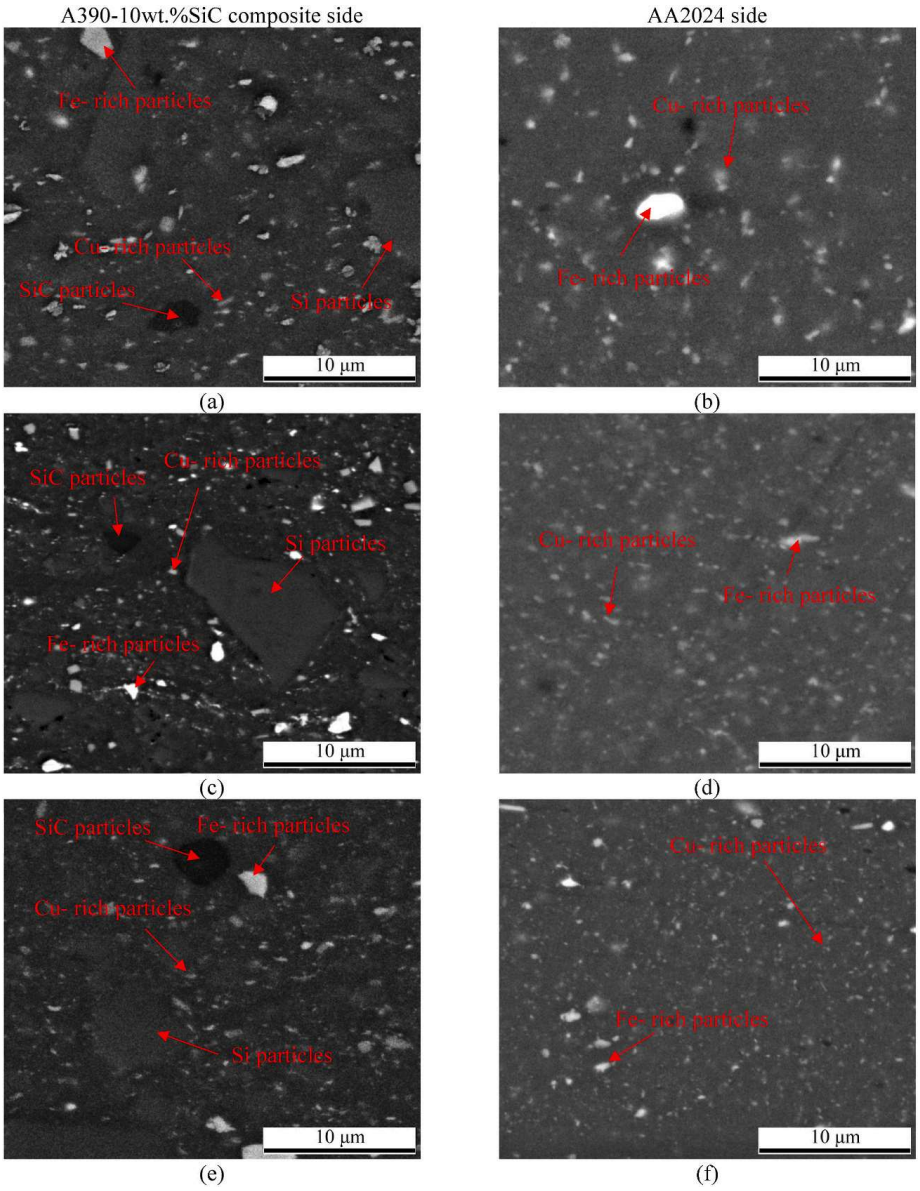

Fig. 6. SEM image of; a) sample V-40, b) sample V-60, c) sample V-80.

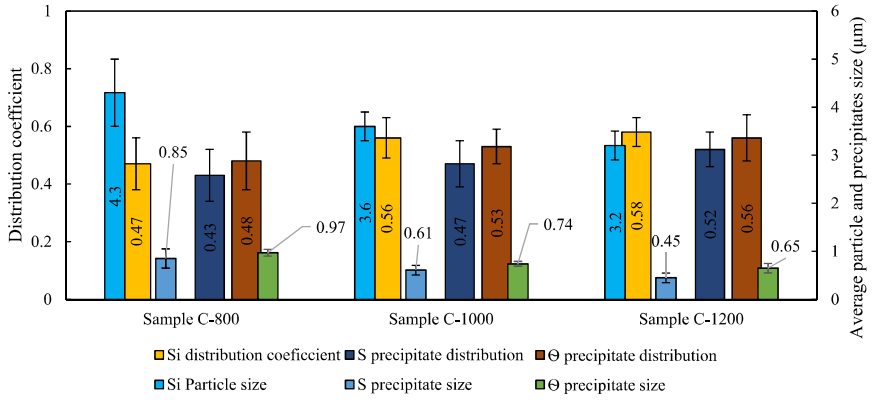

Fig. 7. The distribution coefficient and size of different particles and precipitates in different samples.

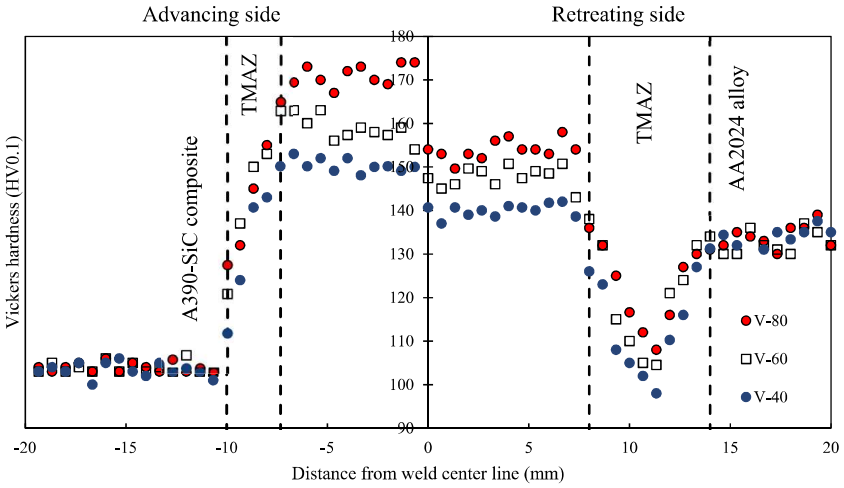

Fig. 8. The microhardness profile in midsection of different samples.

zone. This leads to increased strength, decreased EP, and increased area under the stress-strain (S–S) curve, which represents the SZ toughness. Enhancing the traverse speed from 40 to 80 mm/min yield strength values will result in a 10.3 and 8.4% increase in UTS and a 5.8% decrease in EP. Decreased grain boundary (GB) and increased grain size result in a reduction in the effectiveness of GB strengthening, also known as Hall-Petch strengthening [25]. It follows that a higher level of strength and hardness should be expected in the smaller-grained sample.

Besides, precipitate sizes, SPPs, and smaller carbide and Si particles form in the SZ with increasing traverse speed. The contribution of SPP strengthening rises as precipitates and particles get smaller. The sample welded at an 80 mm/min traverse speed is expected to exhibit a greater effectiveness degree of SPP strengthening mechanism. Reducing particle size and increasing cooling rate increases the effectiveness of the CTE difference strengthening mechanism based on [26], where this mechanism has been discussed. Smaller carbide and Si particles form in the SZ by increasing the traverse speed, according to the microstructural images. Additionally, the cooling rate rises due to the joint area receiving less heat input due to increased traverse speed, leading to an improvement in the contribution of the CTE difference strengthening. Based on the microstructural images, a sound, seamless interface forms in the SZ of all the welded samples between Si carbide and Si particles with an Al matrix. Under these circumstances, the welded samples' SZ load transfer strengthening mechanisms should not significantly differ in terms of effectiveness. Fig. 10(a–e) and 11 (a-c) display the longitudinal and transverse tensile test samples' fracture surfaces. The fracture surface in transverse tensile samples exhibits a brittle fracture morphology, signifying that the fracture occurred in the vicinity of the base metal and was not impacted by plastic strain. Large aspect ratio (~5) eutectic Si particles (shown by blue arrows) are one of the primary factors contributing to failure in this zone, as indicated by indented surfaces on the fracture surface. In the tensile test, this causes stress concentration, which in turn causes crack growth and nucleation, and consequently, low strength and elongation for the transverse tensile test samples. Conversely, the longitudinal tensile test samples have ductile fractures with a dimpled fracture surface. This is because equiaxed particles and refined equiaxed grains form (shown by red arrows), leading to high elongation and ductile fracture surface in the S–S curves.

The results of the polarization test for welded samples and base metals are displayed in Fig. 12. It is evident that both samples' welding zones exhibited lower corrosion current and a shift in corrosion voltage toward nobler values in comparison to the composite base metal. In the meantime, the voltage and corrosion current of the welded samples increased in comparison to the AA2024 base metal. Additionally, the corrosion current rises from 0.0202 to 0.0304 mA cm^{-2} when the traverse speed is reduced from 80 to 40 mm/min. The relations described in Refs. [27,28] are used to calculate the corrosion rates of various samples listed in Fig. 13. Welding corrosion resistance is shown to rise for the composite and fall for the AA2024 base metals. It has been observed that after friction stir processing (FSP), the corrosion resistance is reduced for the AA2024 Al alloy and improved for the Al–Si cast alloys [29,30]. This may be explained by the precipitate concentration in the GBs of the AA2024 Al alloy, the development of coarse precipitates, and the elimination of casting defects in cast alloys. Fig. 14(a–b) displays the EIS results for the various samples. As shown, the Nyquist plots of various samples exhibit both an inductive and a capacitive ring. Reduced electron exchange at the surface and improved corrosion resistance are the results of increased surface passive layer density, material flow in the SZ, and SPD-based defect removal, as demonstrated by the welded samples' larger capacitor ring diameter in comparison with the composite base metal sample [31]. The reduced corrosion resistance of the welded samples' SZ in comparison to the AA2024 base metal and reduced capacitor ring diameter result from the formation of Cu-rich GB precipitates and emptying of GB areas [32]. The capacitor ring diameter decreases in comparison to the welded sample at an 80 mm/min traverse speed due to increased Cu-free GB area brought on by increasing heat input during the welding process.

Examining the Bode plot shown in Fig. 14 (b) shows unique weld area impedance properties. It should be noted that the weld area shows a higher impedance value than the composite base metal and a lower impedance value than the AA2024 base metal at lower frequencies. Low-frequency impedance values significantly increase with increasing traverse speed, which suggests improved

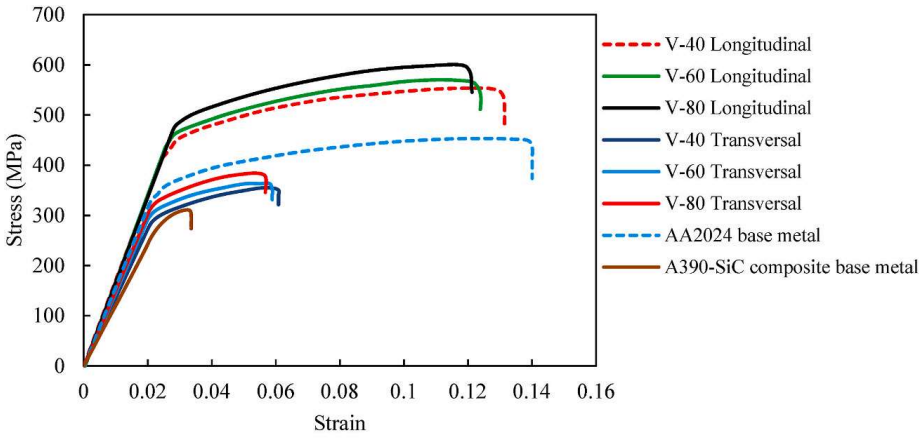

(a)

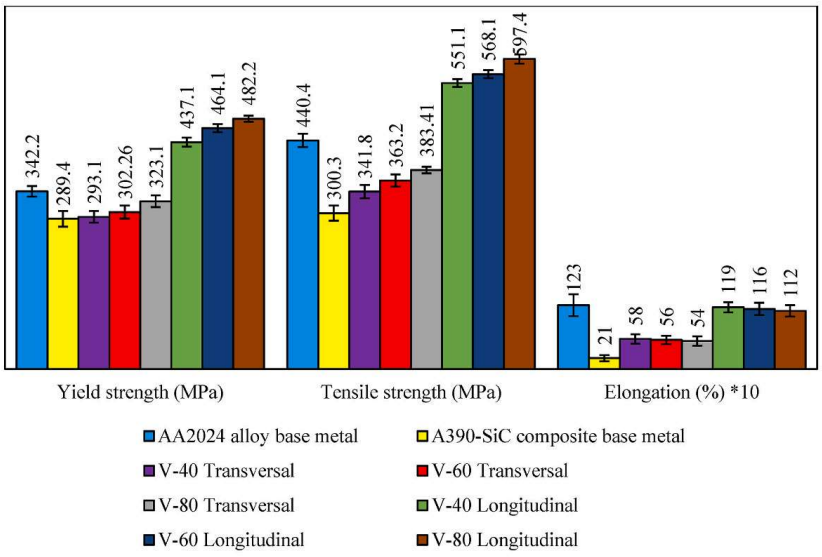

(b)

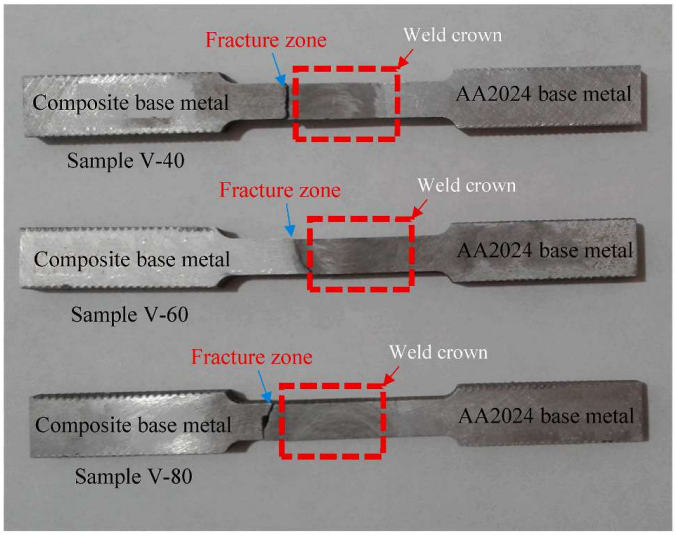

(c)

Fig. 9. a) stress-strain curve of different samples, b) tensile test results, c) fracture zone of the transverse tensile samples.

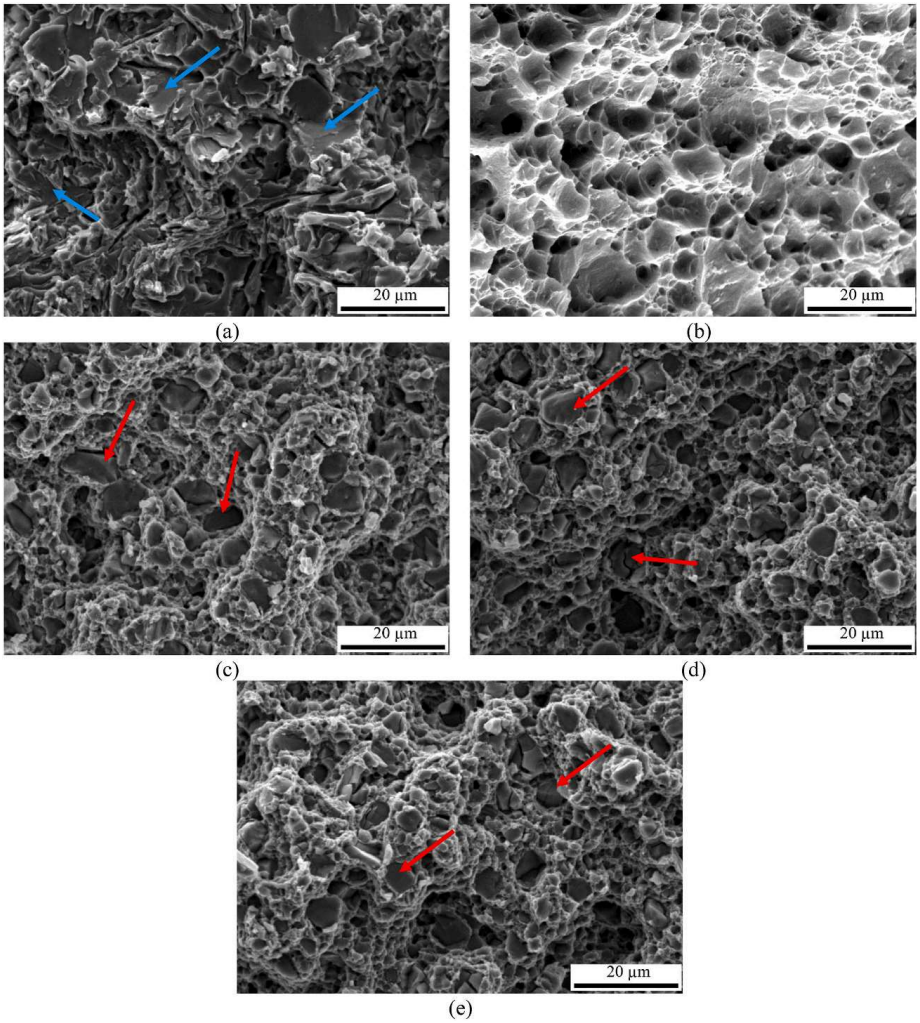

Fig. 10. SEM image of fracture surface of longitudinal tensile sample of; a) sample V-40, b) sample V-60, c) sample V-80, d) A390-SiC composite base metal, e) AA2024 aluminum alloy base metal.

corrosion resistance. Table 1 provides a summary of the comprehensive findings from the equivalent circuit. As indicated, as the traverse speed increases, R_t values rise as well, which correlate with one another in comparison with the corrosion resistance determined by the polarization test. Fig. 15(a–e) illustrates the images of the corrosion surfaces of various samples. Even though the composite base metal experiences severe galvanic corrosion, the corrosion intensity is reduced as traverse speed increases, finer precipitates form, and SPPs are distributed uniformly. The crucial difference is that the welded samples and composite base metal exhibit lower corrosion resistance than the AA2024 base metal.

4. Conclusion

The study examined the effects of varying the traverse speed of the FSW tool on the microstructure, corrosion resistance, and mechanical properties of dissimilar A390-10 wt% SiC composite-AA2024 Al alloy joints. The following conclusions were drawn from this research.

- With a minimum traverse speed of 40 mm/min, the welded sample displays the laminar flow of the two materials in the SZ.
- During the process, large aspect ratio eutectic Si particles were broken under the applied strain, resulting in their reduced aspect ratio. Despite their polygonal morphology and relatively constant aspect ratio, primary Si particles only fracture and fragment into smaller particles.
- The AS has smaller grain sizes than the RS in each of the three samples. The grain size was reduced by up to 71% due to increased plastic strain and reduced particle size in the SZ, which occurred when the traverse speed decreased from 80 to 40 mm/min and the temperature increased.
- Reduced traverse speed, elevated SZ temperature, and slowed joint cooling rate caused SZ precipitates to grow and exhibit greater size than those in the SZ of the sample welded at the highest traverse speed (80 mm/min).

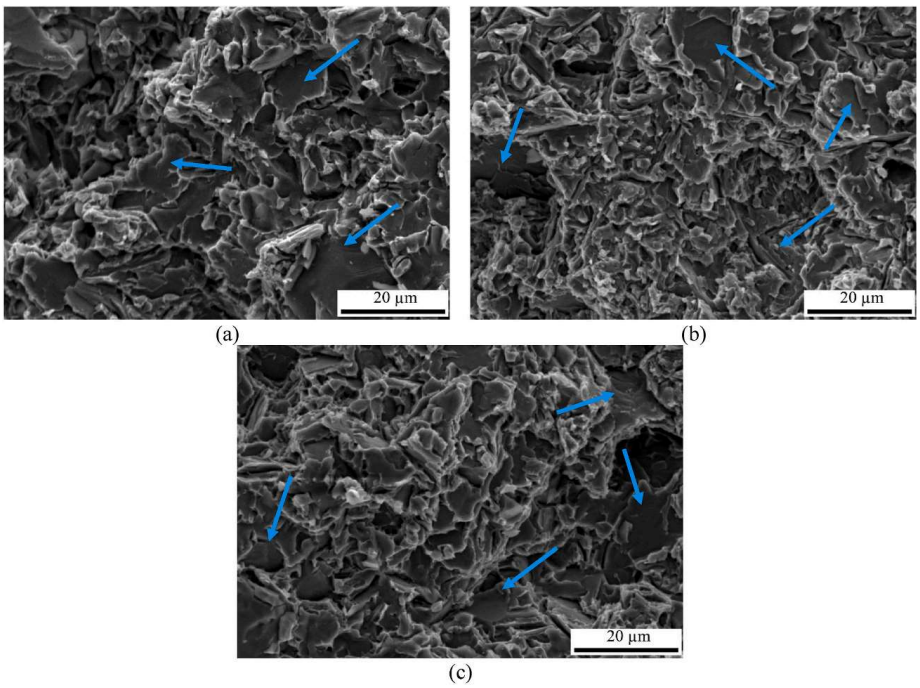

Fig. 11. SEM image of fracture surface of transversal tensile sample of; a) sample V-40, b) sample V-60, c) sample V-80.

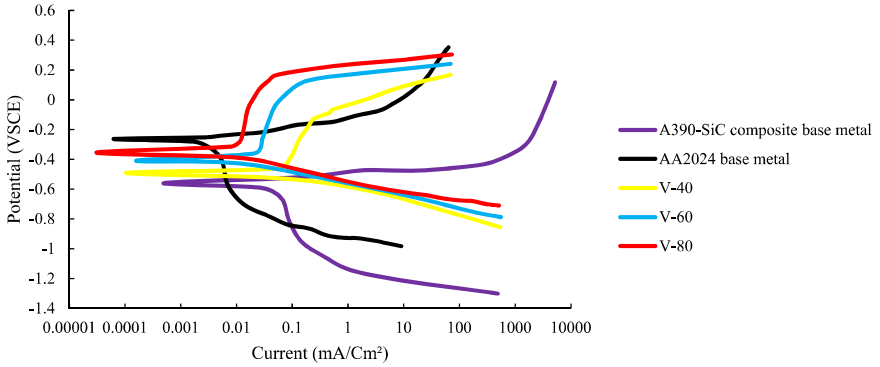

Fig. 12. Polarization curves of different samples.

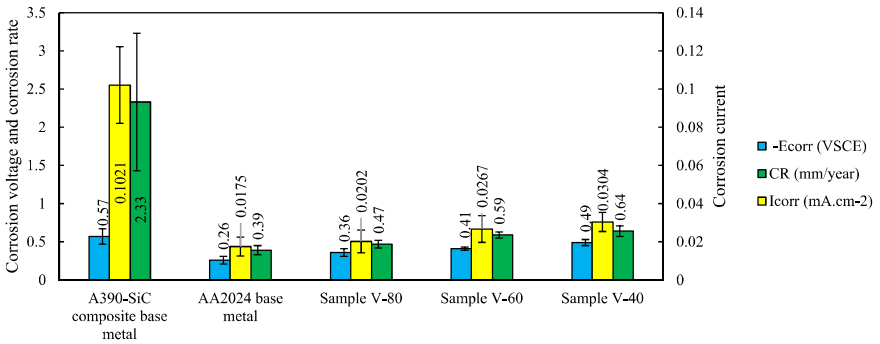

Fig. 13. The corrosion voltage, current and corrosion rate of different samples.

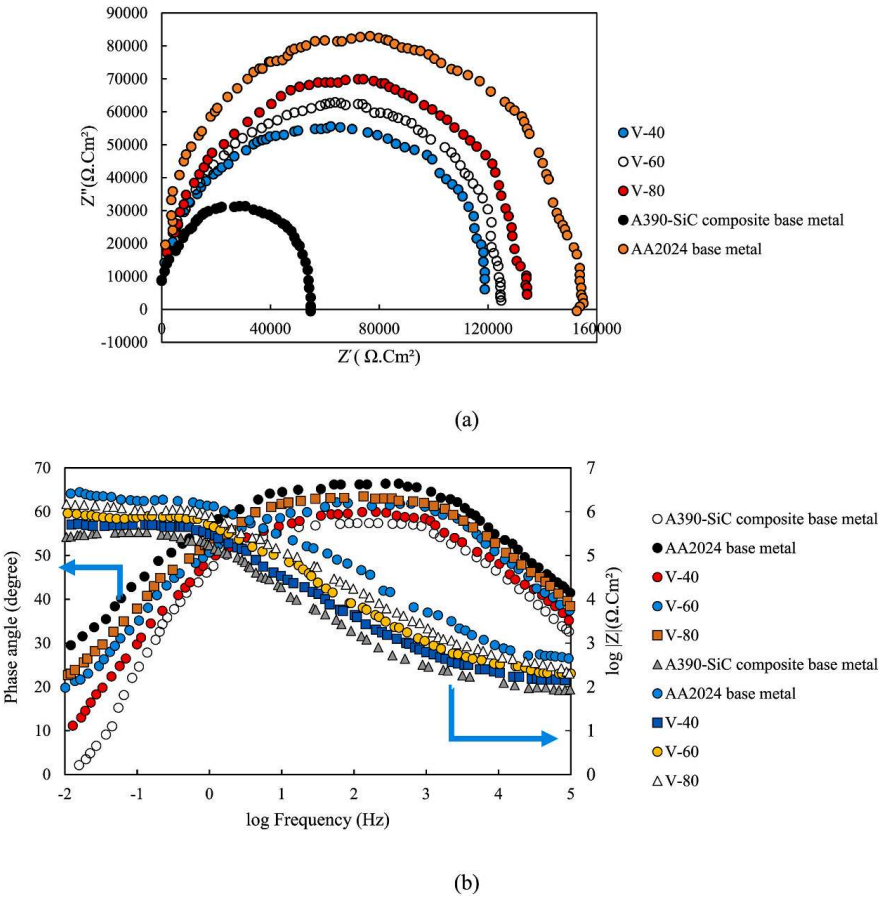

Fig. 14. a) Nyquist diagram, b) Bode and phase plots of different samples.

Table 1
The measurements made after fitting the experimental EIS data.

Sample no.	Rs ($\Omega.cm^2$)	C_{dl} ($F.cm^{-2}$)	n	R_{ct} ($\Omega.cm^2$)	L ($Henri.cm^{-2}$)	R_l ($\Omega.cm^2$)	R_t ($\Omega.cm^2$)
Composite base metal	74.21	5.98×10^{-6}	0.55	5.46×10^{4}	2.98×10^{6}	502.12	5.96×10^{4}
AA2024 base metal	89.12	3.29×10^{-6}	0.89	15.32×10^{4}	1.05×10^{6}	351.23	15.67×10^{4}
V-40	80.21	4.21×10^{-6}	0.80	9.15×10^{4}	2.23×10^{6}	465.32	10.01×10^{4}
V-60	81.56	4.01×10^{-6}	0.83	11.14×10^{4}	2.11×10^{6}	454.21	11.03×10^{4}
V-80	82.78	3.43×10^{-6}	0.85	12.51×10^{4}	1.56×10^{6}	433.11	11.89×10^{4}

- The mean size of Si particles dropped from 7.4 to 5.9 μm as shear stress on the material and traverse speed increased (from 40 to 80 mm/min) in the SZ.
- When the traverse speed was increased from 40 to 80 mm/min for the yield strength, the EP dropped by 5.8% and the UTS increased by 10.3% and 8.4%, respectively.
- The voltage and corrosion current of the welded samples were higher than those of the AA2024 base metal. The corrosion current also increased from 0.0202 to 0.0304 mA cm^{-2} when the traverse speed was reduced from 80 to 40 mm/min.

Ethical statement

Authors state that the research was conducted according to ethical standards.

Data availability statement

Data will be made available on request.

CRediT authorship contribution statement

Hamed Jamshidi Aval: Writing – review & editing, Writing – original draft, Supervision, Methodology, Investigation,

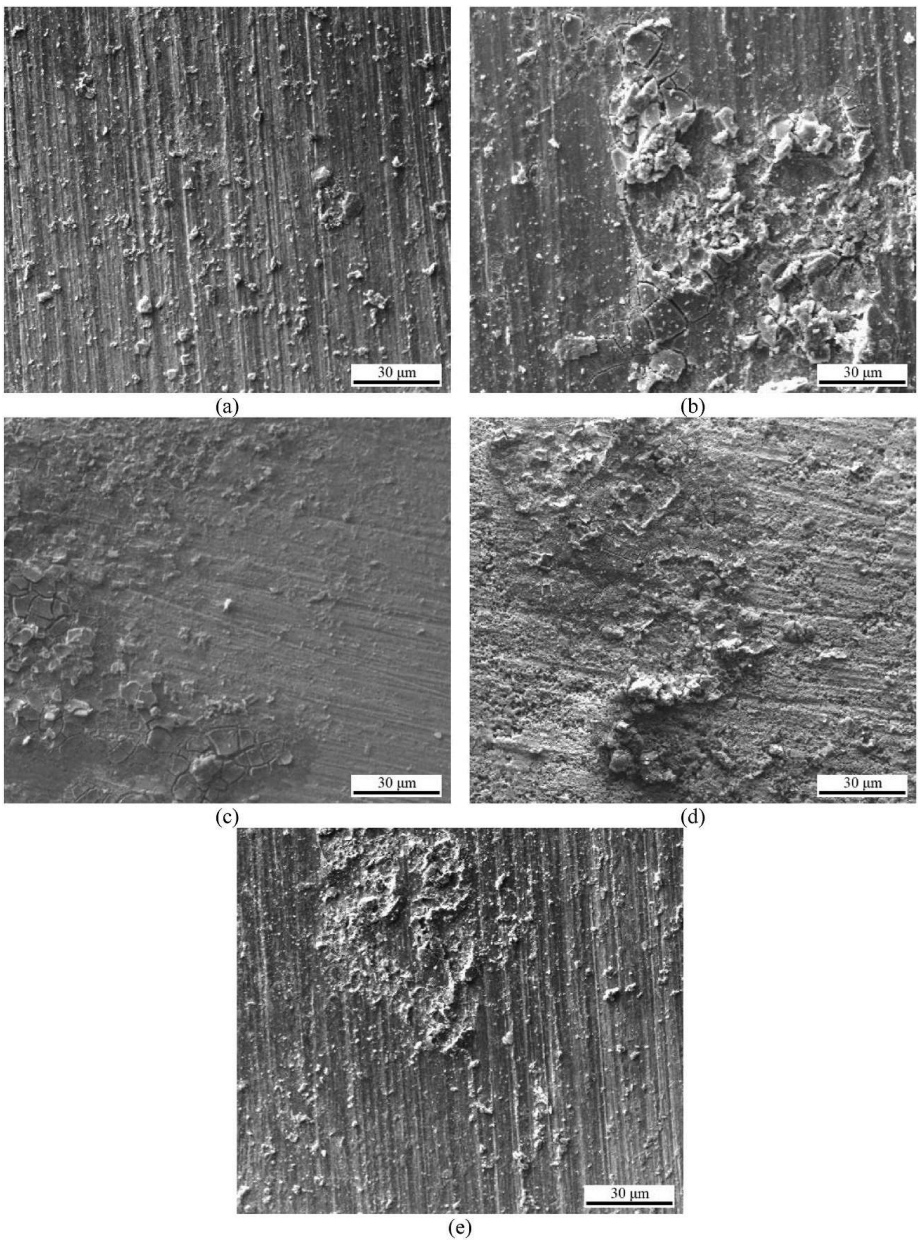

Fig. 15. The SEM images of corrosion surface of samples; a) A390-SiC composite base metal, b) AA2024 base metal, c) sample V-40, d) sample V-60, e) sample V-80.

Conceptualization. **Ivan Galvão:** Writing – review & editing, Investigation.

Declaration of competing interest

The authors declare that they have no known competing financial interests or personal relationships that could have appeared to influence the work reported in this paper.

References

[1] U. Acharya, B.S. Roy, S.C. Saha, Effect of tool rotational speed on the particle distribution in friction stir welding of AA6092/17.5 SiCp-T6 composite plates and its consequences on the mechanical property of the joint, Defence Technology 16 (2) (2020) 381–391.
[2] M. Amirizad, A.H. Kokabi, M.A. Gharacheh, R. Sarrafi, B. Shalchi, M. Azizieh, Evaluation of microstructure and mechanical properties in friction stir welded A356+15%SiCp cast composite, Mater. Lett. 60 (4) (2006) 565–568.
[3] Y. Bozkurt, A. Kentli, U. Hüseyin, S. Salman, Experimental investigation and prediction of mechanical properties of friction stir welded aluminium metal matrix composite plates, Mater. Sci. 18 (4) (2012) 336–340.
[4] B.A. Kumar, N. Murugan, Optimization of friction stir welding process parameters to maximize tensile strength of stir cast AA6061-T6/AlNp composite, Mater. Des. 57 (2014) 383–393.
[5] O.S. Salih, H. Ou, X. Wei, W. Sun, Microstructure and mechanical properties of friction stir welded AA6092/SiC metal matrix composite, Mater. Sci. Eng. 742 (2019) 78–88.

[6] N. Kaushik, S. Singhal, A case study of mechanical and metallurgical properties of friction stir welded AA6063 AMC, Int. J. Microstruct. Mater. Prop. 13 (3–4) (2018) 240–255.
[7] D. Kumar, D.J. Ottarackal, U. Acharya, T. Medhi, B. Saha Roy, S.C. Saha, A parametric study of friction stir welded AA6061/SiC AMC and its effect on microstructure and mechanical properties, Mater. Today: Proc. 46 (2021) 9378–9386.
[8] K. Kalaiselvan, I. Dinaharan, N. Murugan, Characterization of friction stir welded boron carbide particulate reinforced AA6061 aluminum alloy stir cast composite, Mater. Des. 55 (2014) 176–182.
[9] S. Gopalakrishnan, N. Murugan, Prediction of tensile strength of friction stir welded aluminium matrix TiCp particulate reinforced composite, Mater. Des. 32 (1) (2011) 462–467.
[10] A.M. Hassan, M. Almomani, T. Qasim, A. Ghaithan, Effect of processing parameters on friction stir welded aluminum matrix composites wear behavior, Mater. Manuf. Process. 27 (12) (2012) 1419–1423.
[11] J.-w. Zhao, S.-s. Wu, Microstructure and mechanical properties of rheo-diecasted A390 alloy, Trans. Nonferrous Metals Soc. China 20 (2010) s754–s757.
[12] J. Mohamadigangaraj, S. Nourouzi, H.J. Aval, Microstructure, mechanical and tribological properties of A390/SiC composite produced by compocasting, Trans. Nonferrous Metals Soc. China 29 (4) (2019) 710–721.
[13] C. Zhang, G. Huang, Y. Cao, Y. Zhu, X. Huang, Y. Zhou, Q. Li, Q. Zeng, Q. Liu, Microstructure evolution of thermo-mechanically affected zone in dissimilar AA2024/7075 joint produced by friction stir welding, Vacuum 179 (2020) 109515.
[14] S. Lin, J. Tang, S. Liu, Y. Deng, H. Lin, H. Ji, L. Ye, X. Zhang, Effect of travel speed on microstructure and mechanical properties of FSW joints for Al–Zn–Mg alloy, Materials 12 (24) (2019) 4178.
[15] L. Fratini, G. Buffa, CDRX modelling in friction stir welding of aluminium alloys, Int. J. Mach. Tool Manufact. 45 (10) (2005) 1188–1194.
[16] P. Yu, C. Wu, L. Shi, Analysis and characterization of dynamic recrystallization and grain structure evolution in friction stir welding of aluminum plates, Acta Mater. 207 (2021) 116692.
[17] Q. Chu, W. Li, D. Wu, X. Liu, S. Hao, Y. Zou, X. Yang, A. Vairis, In-depth understanding of material flow behavior and refinement mechanism during bobbin tool friction stir welding, Int. J. Mach. Tool Manufact. 171 (2021) 103816.
[18] A.N. Albakri, B. Mansoor, H. Nassar, M.K. Khraisheh, Thermo-mechanical and metallurgical aspects in friction stir processing of AZ31 Mg alloy—a numerical and experimental investigation, J. Mater. Process. Technol. 213 (2) (2013) 279–290.
[19] D. Andrade, C. Leitão, N. Dialami, M. Chiumenti, D. Rodrigues, Analysis of contact conditions and its influence on strain rate and temperature in friction stir welding, Int. J. Mech. Sci. 191 (2021) 106095.
[20] N.Z. Khan, D. Bajaj, A.N. Siddiquee, Z.A. Khan, M.H. Abidi, U. Umer, H. Alkhalefah, Investigation on effect of strain rate and heat generation on traverse force in FSW of dissimilar aerospace grade aluminium alloys, Materials 12 (10) (2019) 1641.
[21] C. Chang, C. Lee, J. Huang, Relationship between grain size and Zener–Holloman parameter during friction stir processing in AZ31 Mg alloys, Scripta Mater. 51 (6) (2004) 509–514.
[22] M. Araghchi, H. Mansouri, R. Vafaei, Influence of cryogenic thermal treatment on mechanical properties of an Al–Cu–Mg alloy, Mater. Sci. Technol. 34 (4) (2018) 468–472.
[23] I. Dutta, C. Harper, G. Dutta, Role of Al 2 O 3 particulate reinforcements on precipitation in 2014 Al-matrix composites, Metall. Mater. Trans. 25 (1994) 1591–1602.
[24] Y. Zhou, H. Xiong, Y. Zhang, C. Kong, H. Yu, Microstructure and mechanical properties of ultrafine-grained AA2024 sheets joined by underwater friction stir welding, Mater. Char. 198 (2023) 112749.
[25] N.Q. Chinh, D. Olasz, A.Q. Ahmed, G. Sáfrán, J. Lendvai, T.G. Langdon, Modification of the Hall-Petch relationship for submicron-grained fcc metals, Mater. Sci. Eng. 862 (2023) 144419.
[26] L.H. Dai, Z. Ling, Y.L. Bai, Size-dependent inelastic behavior of particle-reinforced metal–matrix composites, Compos. Sci. Technol. 61 (8) (2001) 1057–1063.
[27] A. Bordbar-Khiabani, B. Yarmand, M. Mozafari, Enhanced corrosion resistance and in-vitro biodegradation of plasma electrolytic oxidation coatings prepared on AZ91 Mg alloy using ZnO nanoparticles-incorporated electrolyte, Surf. Coating. Technol. 360 (2019) 153–171.
[28] K. Tahmasbi, M. Mahmoodi, H. Tavakoli, Corrosion resistance of aluminum alloy AA7022 wire fabricated by friction stir extrusion, Trans. Nonferrous Metals Soc. China 29 (8) (2019) 1601–1609.
[29] M.M. Jalilvand, Y. Mazaheri, A. Heidarpour, M. Roknian, Development of A356/Al2O3 + SiO2 surface hybrid nanocomposite by friction stir processing, Surf. Coating. Technol. 360 (2019) 121–132.
[30] M. Jariyaboon, A.J. Davenport, R. Ambat, B.J. Connolly, S.W. Williams, D.A. Price, The effect of welding parameters on the corrosion behaviour of friction stir welded AA2024–T351, Corrosion Sci. 49 (2) (2007) 877–909.
[31] H. Feng, S. Liu, Y. Du, T. Lei, R. Zeng, T. Yuan, Effect of the second phases on corrosion behavior of the Mg-Al-Zn alloys, J. Alloys Compd. 695 (2017) 2330–2338.
[32] V. Guillaumin, G. Mankowski, Localized corrosion of 2024 T351 aluminium alloy in chloride media, Corrosion Sci. 41 (3) (1998) 421–438.